Nested potassium hydroxide etching and protective coatings for silicon-based microreactors

Nuria de Mas[1,α], Martin A. Schmidt[2], and Klavs F. Jensen[1,β]

[1]Department of Chemical Engineering and [2]Microsystems Technology Laboratories, Massachusetts Institute of Technology, Cambridge, MA 02139

Short title

Nested KOH etching and protective coatings for microreactors

Abstract

We have developed a multilayer, multichannel microfabricated reactor that uses elemental fluorine as a reagent and generates hydrogen fluoride as a byproduct. Nested potassium hydroxide etching (using silicon nitride and silicon oxide as masking materials) was developed to create a large number of channels (60 reaction channels connected to individual gas and liquid distributors) of significantly different depths (50–650 μm) with sloped walls (54.7º with respect to the (100) wafer surface) and precise control over their geometry. The wetted areas were coated with thermally grown silicon oxide and electron-beam evaporated nickel films to protect them from the corrosive fluorination environment. Up to four Pyrex layers were anodically bonded to three silicon layers in a total of six bonding steps to cap the microchannels and stack the reaction layers. The average pinhole density in as-evaporated films was 3 holes/cm^2. Heating during anodic bonding (up to 350 °C for 4 min)did not significantly alter the film composition. Upon fluorine exposure, nickel films (160 nm thick) deposited on an adhesion layer of Cr (10 nm) over an oxidized silicon substrate (up to 500 nm thick SiO_2) led to the formation of a nickel

[α] Biologics Process Development, Manufacturing Sciences & Technology, Bristol-Myers Squibb Company, 38 Jackson Road, Devens, MA 01434, United States (current affiliation).

[β] Corresponding author. E-mail: kfjensen@mit.edu. Fax: (617) 258-8992.

fluoride passivation layer. This microreactor was used to investigate direct fluorinations at room temperature over several hours without visible signs of film erosion.

1. Introduction

Stand-alone microchemical systems comprising reaction, separation, temperature monitoring, chemical detection, and feedback control may aid chemical research and development by providing new tools to rapidly screen and optimize chemical reactions, catalysts, and materials synthesis. Additionally, small reactor volumes enhance the control of fast, highly exothermic reactions and allow new reaction chemistries deemed difficult to control in conventional macroscopic reactors to be carried out safely [1]. One example of such type of chemistry is the direct fluorination of organic compounds, i.e., the reaction of a precursor molecule with elemental fluorine in an appropriate solvent generating hydrogen fluoride as a byproduct [2, 3].

Over the last decade, a number of microreactors have been developed and fabricated using silicon bulk micromachining techniques. Commonly used silicon etching techniques include KOH etching [4] and deep reactive ion etching (DRIE) [5]. Photolithographically patterning multiple layers on a silicon wafer can be difficult. When the wafer surface has topography with feature depths of several tens of micrometers, it is difficult to spin coat a thin (~1 μm) layer of photoresist with uniform thickness. To address this issue, nested masking techniques use a combination of two masking materials to pattern two different masks defining features that will ultimately have different depths. Nested DRIE using silicon oxide and photoresist as masking materials has been used to build microreactors [6]. More recently, nested KOH etching was reported to achieve convex right-angle corners of merging features using silicon nitride and/or silicon oxide as masking materials [7, 8].

In addition, silicon micromachining permits the patterning of a variety of thin films for use as protective coatings (silicon oxide) [9], heaters (platinum/titanium) [10, 11], temperature (platinum/titanium) [10, 11] and multiphase flow sensors (aluminum) [12], or as structural materials

(silicon nitride) [13, 14]. Silicon micromachining also enables the integration of UV chemical detection [15, 16] and the design of efficient multiphase reactors and separation units [17-19]. Furthermore, arrays consisting of a large number (~100) of microchannels may be operated in parallel in planar and multilayer configurations to increase reactor throughput [19, 20]. Because of the desirable microreactor features enabled by silicon micromachining, we developed a silicon-based microreactor for the synthesis of fluorinated compounds [2].

To build a silicon-based microreactor compatible with the corrosive fluorination environment using silicon and Pyrex as substrate materials, protective coatings chemically compatible with both fluorine and hydrogen fluoride must be applied over all wetted surfaces. Silicon undergoes severe corrosion in the presence of elemental fluorine, forming silicon tetrafluoride (0.2 μm/min in 25 vol % F_2/N_2 at room temperature and atmospheric pressure) [14]. Because silicon oxide was stable at these etching conditions, this etch rate was measured in silicon samples that were soaked for 2 min in a 50:1 solution of H_2O/49 wt % HF to remove the native silicon oxide prior to exposure to fluorine. Silicon oxide is thermodynamically unstable with respect to the reaction with fluorine although this reaction is slow at room temperature in the absence of hydrogen fluoride [21]. Silicon oxide, however, etches readily in the presence of anhydrous and aqueous HF (approximately 100 nm/min in buffered aqueous HF, i.e., 7:1 water/49 wt % HF).

Materials used to handle fluorine in macroscopic systems (e.g., valves, pipes, and pressure regulators) include aluminum, copper, stainless steel, nickel, brass, and nickel alloys such as Inconel, and Monel. The resistance of these materials to fluorine is conferred by the formation of a passivation fluoride layer on the metal upon first contact with fluorine [22]. Materials resistant to HF include aluminum, carbon, austenitic and nickel-chrome steels, copper (in the absence of moisture and air) [23], nickel, Inconel, and Monel. Similarly, these metals form corrosion-resistant fluoride films in contact with HF. Other than these metals, only highly fluorinated polymers, such as polytetrafluoroethylene

(PTFE), show good resistance to F_2 (at least in dilute concentrations) and HF. PTFE, however, is not completely impermeable; if this material is to be used in a protective layer, sufficient thickness must be provided [21, 22, 24].

Several microfabrication techniques are available to deposit metallic thin films, including electron-beam (e-beam) evaporation and sputter deposition [25]. For example, nickel, aluminum, and copper, with thickness of up to approximately 1 μm, are commonly deposited by e-beam evaporation. Sputtered tantalum oxide thin films were reported for use as protective coatings in the packaging of microfabricated sensors (e.g., piezoresistive pressure sensors) [26]. These techniques may be complemented with electroless and electrolytic metal plating to deposit thicker metallic coatings or create entirely metallic structures. Here, we describe a silicon-based fabrication process to create a direct fluorination microreactor consisting of a large number of microfluidic channels with significantly different depths (50–650 μm) by nested KOH etching as an inexpensive alternative to DRIE using low-stress silicon nitride and silicon oxide as masking materials. Thermally grown silicon oxide was selected as a first corrosion barrier against fluorine, and e-beam evaporated nickel provided additional protection against both fluorine and hydrogen fluoride.

2. Experimental

2.1. Fabrication Strategy

To carry out direct fluorination reactions in a microreactor, a gaseous fluorine/nitrogen mixture and an organic liquid solution were continuously fed to the microchannels through separate gas and liquid inlet ports and contact in the device. Our microreactors were operated at ambient temperature and nearly atmospheric pressure in the annular-dry flow regime, where a gas core flows in the center of the channel and liquid wets the walls except for part of the Pyrex [2, 19]. At these operating conditions, the reaction plane is expected to be located close to the gas–liquid interface. Once generated at the reaction plane,

the byproduct HF (normal boiling point of 19.5 °C) will remain partly dissolved in the liquid phase and diffuse towards the channel walls. HF may also be carried into the device by the gaseous fluorine mixture. To minimize the formation of HF from water and thus maximize the lifetime of both the macroscopic fluorine delivery manifold and the microreactor, the entire gas and liquid manifolds were maintained scrupulously dry and all liquid solutions were thoroughly dried with activated molecular sieves prior to fluorination.

We have built and investigated fluorinations in two silicon-based microreactors [2, 20]. Figure 1 (a) shows the configuration of a planar, dual-channel reactor that consists of two microfluidic channels with triangular cross section operating in parallel. The channels are formed on the front side of a silicon substrate and capped by Pyrex. Gas and liquid reagents are fed to the channels through fluidic ports etched on the back side of the silicon. A cross sectional scanning electron micrograph of the channel region is shown in Figure 1 (b). The second reactor, illustrated in Figure 1 (c), is a multilayer design that consists of several alternatively stacked silicon and Pyrex layers [2, 20]. Twenty reaction channels are formed on each silicon layer and capped by Pyrex. A series of flow distributors are used to controllably feed the gas and liquid to the reaction channels in the stack.

Photolithographic silicon bulk micromachining and KOH etching were employed to form all microfluidic channels as well as the gas and liquid inlet and outlet fluidic ports. For the dual-channel reactor, one single etch and three masks (two to pattern the silicon and one to make the shadow mask) were used. For the scaled-out reactor, nested etching (four etches) and six masks (four to pattern the silicon and two to make the shadow masks) were used. Silicon oxide was then thermally grown on the silicon as a first protective layer. Nickel thin films were evaporated over the wetted areas of the silicon and Pyrex cap as defined by the shadow masks as a second protective layer. To facilitate the step coverage of the evaporated films, microchannels with sloped walls etched in KOH (54.7º with respect to the (100) wafer surface) were chosen. Finally, the silicon was anodically bonded to the Pyrex to cap the

channels. For flow visualization studies, nickel coatings were not deposited to allow optical access to the reaction channels through the Pyrex.

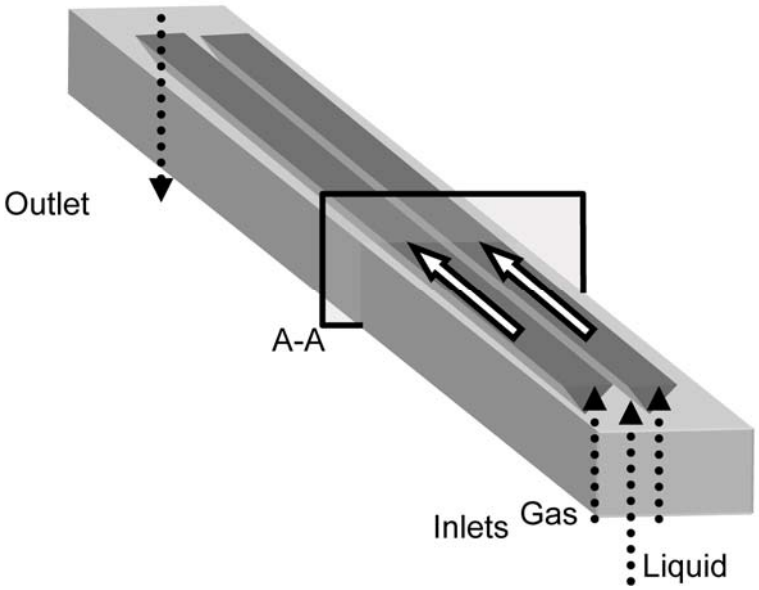

(a)

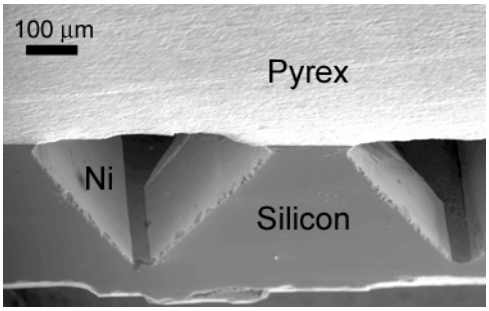

(b)

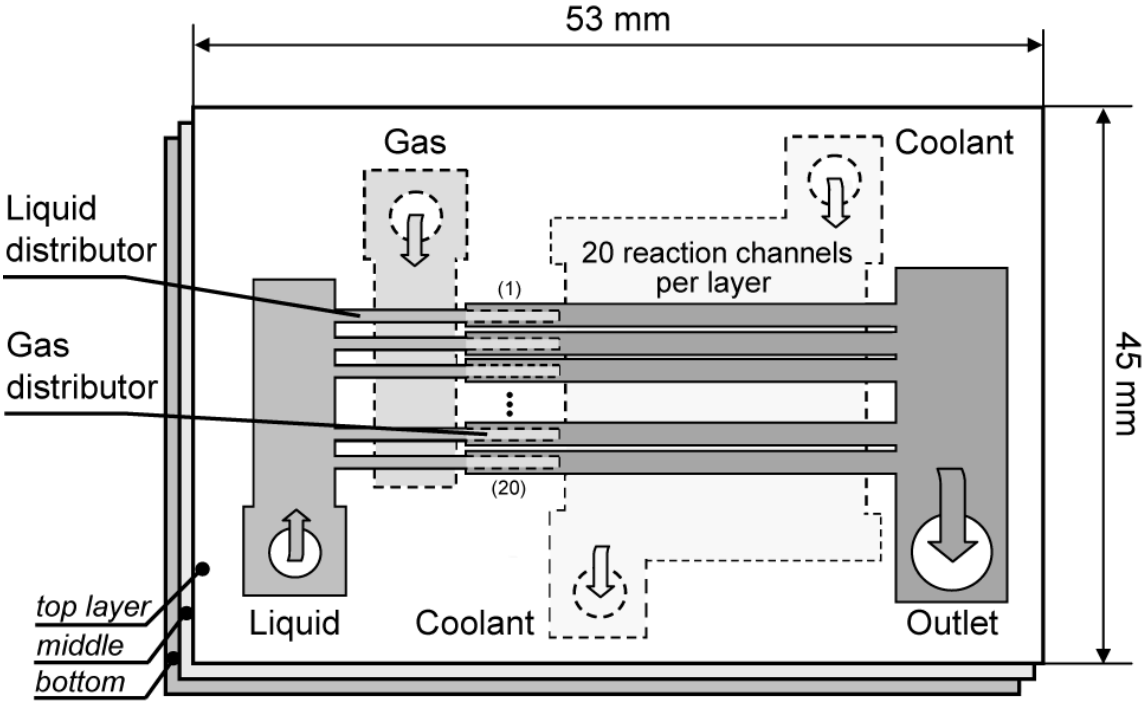

(c)

Figure 1. Schematic of direct fluorination microreactors: (a) planar, dual-channel design; (b) scanning electron micrograph of cross section A-A indicated in (a) showing two reaction microchannels formed in silicon and coated with Ni (200 nm)/Cr (10 nm); (c) multilayer, multichannel design.

2.2. Channel Fabrication Using Nested KOH Etching

The fabrication sequences to create the dual-channel and scaled-out reactors have been briefly described elsewhere [2, 20]. Here we elaborate on the detailed processing steps developed to build these devices. The fabrication of the dual-channel device is shown in Figure 2. It started by depositing low-stress silicon nitride (100 nm thick) by low-pressure chemical vapor deposition (LPCVD) on the front and back sides of a double-polished (100) silicon wafer (100 mm in diameter, 525 μm thick) for use as a masking material during the KOH etch. The front side of the silicon wafer was photolithographically patterned to define the reaction channels (width W = 400 μm, length L = 2 cm, terminated triangular cross section). The exposed silicon nitride (i.e., not protected by photoresist) was then etched using a standard dry etch (CF_4 and O_2 plasma). Inlet and outlet fluidic ports to the reaction channels were patterned on the back side in a similar manner. The reaction channels and ports were then simultaneously etched in an aqueous solution of KOH (20 wt %, 80 °C, 4 drops of surfactant FC-129 per L of water; FC-129 from 3M, MN; 4.0 h). The silicon nitride mask was then removed using a dry or wet (hot phosphoric acid) etch.

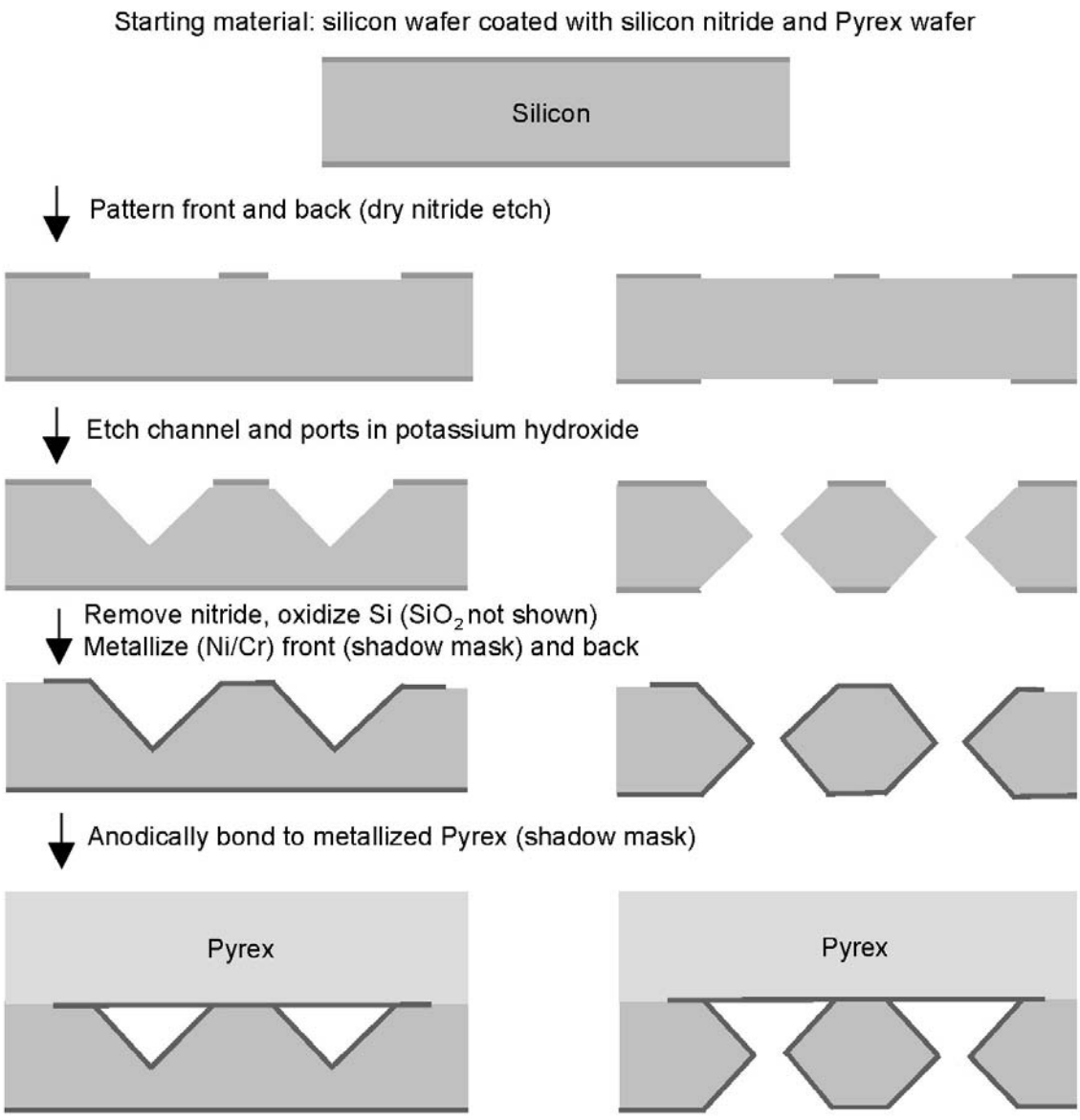

Figure 2. Schematic representation of the microfabrication sequence for the dual-channel reactor: (a) channel cross section and (b) ports cross section.

Patterning each silicon layer of the scaled-out reactor required four photolithographic masks: one mask to pattern the liquid inlet slit and reaction channels on the front side; one mask to pattern the liquid distributors on the front side; one mask to pattern the liquid inlet port, gas inlet port and slit, gas access ports to the reaction channels, outlet slit, and cooling slits on the back side; and one mask to pattern the

gas distributors and cooling channels on the back side. All photolithographic masks except for the liquid-distributors mask were fabricated by laser writing the desired features onto a transparent Mylar film (0.18 mm thick) with a resolution of 13 μm (Photoplot Store, CO), and then photolithographically transferring these features onto a chromium-coated soda-lime glass plate. The liquid distributors (W = 71 μm, the smallest features of the device) were patterned using a laser-written photomask with a resolution of 3 μm (Advance Reproductions Corp., MA).

The microfabrication sequence to form the liquid inlet slit, reaction channels, and liquid distributors is schematically illustrated in Figure 3. Low-stress silicon nitride (100 nm thick) was first deposited by LPCVD on the front and back sides of a double-polished (100) silicon wafer (150 mm in diameter, 650 μm thick). The nitride layer on the front side was photolithographically patterned (positive resist and clear field mask) to define the inlet slit and reaction channels. The exposed nitride (i.e., not protected by photoresist) was etched using a dry etch (CF_4 and O_2 plasma), and a layer of silicon oxide (0.8 μm thick) was thermally grown for use as a masking material during the first KOH etch (step 1). The silicon oxide was then photolithographically patterned (positive resist and dark field mask) to define the distributors. Only 100 nm thick, the silicon nitride patterns did not interfere with the spin coating of photoresist (~1 μm thick) over the wafer. The exposed oxide was etched in buffered oxide etchant (BOE, step 2). The distributors were then etched in an aqueous solution of KOH (20 wt %, 65 °C, 4 drops FC-129 per L of water; actual etch rate at 65 °C ≈27.3 μm/h; step 3). The remaining silicon oxide was stripped in BOE, and a new layer of silicon oxide was thermally grown (1.3 μm thick, step 4) for use as a masking material in the second KOH etch. The nitride was then stripped using again the same dry etch to uncover the features of the first mask on bare silicon (step 5). The thickness of the silicon-oxide layer did not appreciably change during this nitride etch. Finally, the inlet slit and reaction channels were etched in KOH (15 wt %, 60 °C, 4 drops FC-129 per L water; ≈22.8 μm/h, step 6). The same processing steps were performed on the back side of the silicon wafer following those performed on the front side to form

the gas distributors and cooling channels (third KOH etch), as well as the inlet ports, gas access ports to the reaction channels, outlet slit, and cooling slits (fourth KOH etch). A new layer of low-stress silicon nitride (100 nm thick) deposited on the front side of the wafer served as an etch stop for this fourth etch.

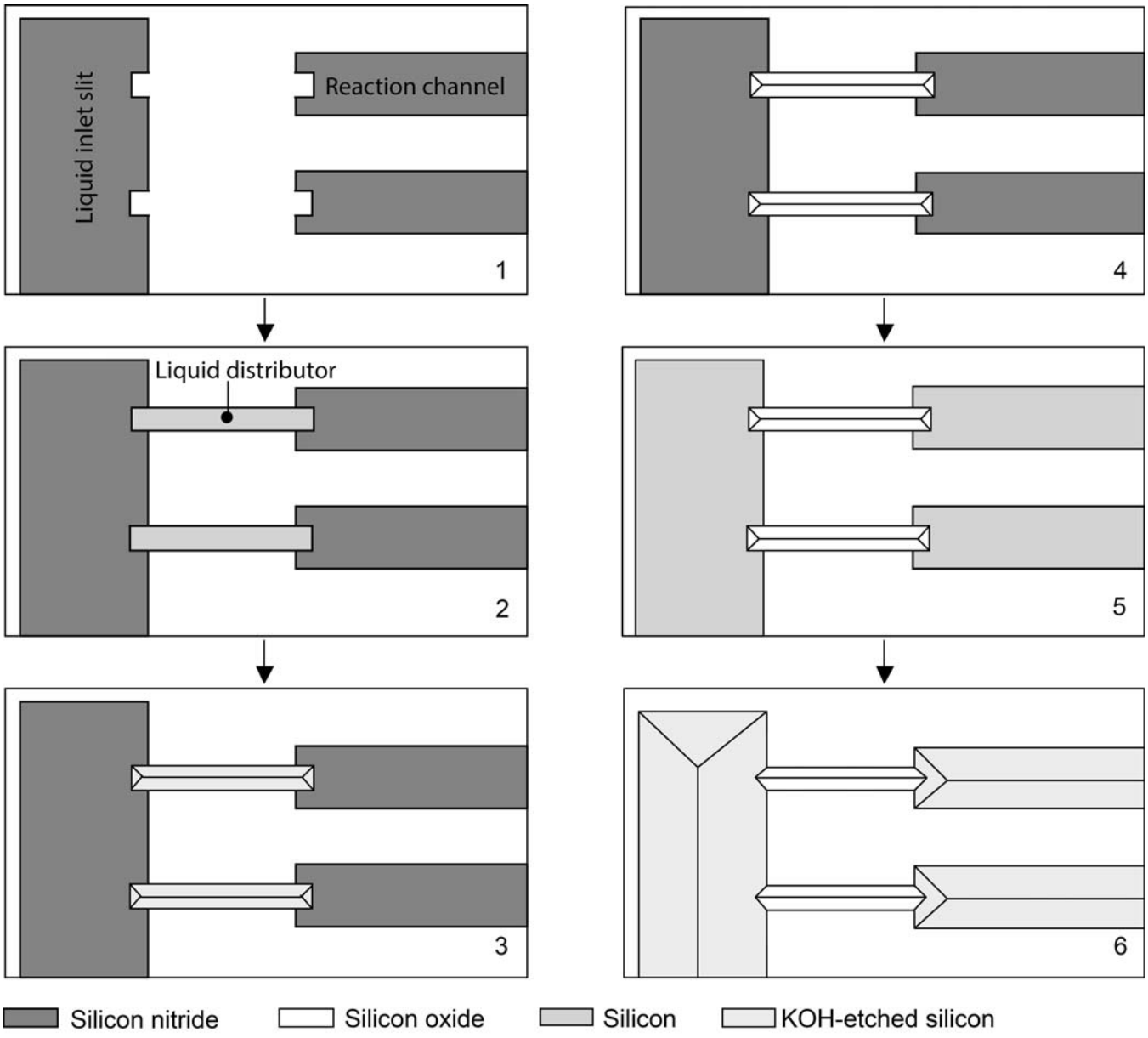

Figure 3. Top view of the microfabrication sequence implemented on the front side of a silicon wafer to create the liquid inlet slit, reaction channels, and liquid distributors by nested KOH etching. The same sequence was used on the back side to form the gas and liquid inlet ports, gas access ports to the reaction channels, outlet slit, cooling slits, gas distributors, and cooling channels.

Etches were carried out in a volume of KOH solution of approximately 4.8 L, and up to two wafers were etched at a time. Each wafer contained four reaction-layer dies. The long (third and fourth) KOH etches on the front and back sides were started simultaneously to reduce the stress on the wafer caused by the uneven thicknesses of the remaining SiO_2 films over its two sides that would otherwise develop as the etching progressed. To save processing time, the nitride layers on the front and back sides of the wafer were patterned first. Next, the gas and liquid distributors and cooling channels were patterned and then etched simultaneously until the etch of the liquid distributors terminated. The wafer was then mounted on a Teflon jig and sealed with O-rings to protect the front side from further etching. The wafer was then brought back into the KOH bath until the etch of the gas distributors and cooling channels terminated.

2.3. Thermal Oxidation of Silicon and E-Beam Evaporation of Nickel Films

After etching all channels, the remaining silicon nitride and silicon oxide were stripped using a dry etch (CF_4 and O_2 plasma) and BOE, respectively, and a new layer of silicon dioxide (250–500 nm thick) was (conformally) grown over the silicon channels at 1,050 ºC by dry-wet-dry oxidation. Wafers to be oxidized were prepared using standard clean room procedures: clean in an ammonium hydroxide/hydrogen peroxide solution, followed by a dip in a 50:1 water:49 wt % hydrogen fluoride solution, and a clean in a hydrochloric acid/hydrogen peroxide solution. In preparation for evaporation, unmetallized wafers were cleaned in a piranha solution (sulfuric acid:30 wt % hydrogen peroxide, 3:1; careful, keep organics away from this mixture). After the first metallization, wafers were cleaned using only organic solvents (acetone, methanol, and isopropanol) because nickel was found to etch in piranha, even in diluted concentration (Nanostrip™).

The front and back sides of the silicon and Pyrex (7740, 150 mm diameter, 762 μm thick) wafers were metallized with nickel (200 nm thick) on an adhesion layer of chromium (10 nm thick) by e-beam evaporation in a Temescal VES-2250 apparatus at a base pressure of $\approx 3.5 \times 10^{-7}$ Torr and deposition

rates of 3 and 1 Å/s, respectively. Wafers were mounted on a flat stage. The description of the Ni/Cr films includes the target metal thickness that was specified during evaporation. For Ni (200 nm)/Cr (10 nm) films, the measured total film thickness was approximately 165 nm. The thickness reported for SiO_2 is the measured value. A shadow mask was used to cover the unwetted areas of the silicon and Pyrex during evaporation because the subsequent anodic bonding required uncoated silicon and Pyrex. The shadow mask was a silicon wafer with openings approximately 200 μm larger per side than the most-outer edges of the wetted areas. KOH etching and DRIE were used to fabricate the shadow masks of the dual-channel and scaled-out reactors, respectively. The high channel density and finite thickness of the silicon wafer precluded the use of KOH etching for the scaled-out reactor.

The fabrication was completed by anodically bonding the silicon and Pyrex (up to 325–350 °C, 800 V, 3–4 min). To create the scale-out reactor, six successive anodic bonding steps were carried out at the die level [27] using three silicon and four mechanically drilled (Ferro-Ceramic Grinding, Inc., MA) Pyrex layers. This completed device was employed for flow visualization studies and thus patterned with aluminum waveguides using a standard lift-off process followed by e-beam evaporation (no Ni was deposited) [20]. For bonding the wafer stacks, electrical contact to the electrically conductive (doped) silicon layer was made through side openings in the Pyrex die. When first brought in contact for alignment, the silicon and Pyrex surfaces formed a small air gap, and interference fringes were visually observed. As a test for the absence of defects or surface contaminants, the fringes disappeared when a small pressure was applied on the contacted surfaces. If fringes remained, the surfaces were cleaned again. When the bond was formed, the fringes disappeared and the interface became dark. The graphite electrode was polished before each bonding step.

2.4. Characterization of Protective Films

Desirable characteristics of the Ni coatings are satisfactory adhesion, low pinhole density, step coverage over the channel walls, self-passivation upon exposure to fluorine and HF, and ability to bond

coated substrates. The morphology and step coverage of the films was examined by scanning-electron microscopy (SEM) using a Philips/FEI XL30 microscope. Film structure was determined by X-ray diffraction using a Rigaku RU300 rotating-anode X-ray generator. Film thickness was measured using a Tencor P10 surface profilometer. Adhesion of the evaporated films was qualitatively measured by the adhesive-tape test, in which a piece of office scotch tape was firmly applied to a nickel-coated surface and then removed. Good adhesion was indicated by the lack of any nickel on the peeled tape [28]. The internal stress of the nickel thin films (σ_T) was obtained by measuring the change in wafer bow caused by film deposition using a Tencor FLX-2320 instrument and the Stoney formula [29]. The pinhole number density in the metallic films was estimated by counting the number of light points visible through a coated Pyrex sample (≈20 cm^2) via transmission optical microscopy using a Zeiss Axiovert 200 microscope and a 40× lens objective with a numerical aperture of 0.75. Chemical analysis of film surfaces by Auger electron spectroscopy (AES) and X-ray photoelectron electroscopy (XPS) was performed using a Physical Electronics Model 660 Scanning Auger Microscope operating at 5.0 kV and a Kratos AXIS Ultra Imaging XPS with an Al Kα source, respectively. Elemental depth-profile analysis was obtained by XPS using an argon-ion sputtering system operating at 5.0 kV; the duration of each sputtering cycle was 120 s.

The chemical resistance of metal-coated samples to elemental fluorine was tested at ambient temperature and pressure in a gas-tight cylindrical chamber (34 mm inner diameter, 38 mm outer diameter, 125 mm length). A 25 vol % mixture of fluorine in nitrogen (Spectra Gases, fluorine purity 99.0%, nitrogen purity 99.9999%, connected to a Monel pressure regulator) was continuously fed to the chamber. The design and operation of the fluorine gas manifold has been previously described [2]. The front and back faces of the chamber were sealed using ultra-high vacuum knife-edge flanges. A quartz window was attached to the front face to allow visual inspection of the sample. The back face was sealed using a copper disc. Small-diameter inlet and outlet tubing (316 stainless steel, 1.6 mm o.d.,

1 mm i.d.) to promote uniform gas distribution inside the chamber was passed through two holes in the disc and fixed with low-vapor-pressure epoxy resin (Varian Torr Seal). The sample was inserted into an aluminum support that was held in the center of the chamber. The outlet stream was fed into a fluorine scrubbing system (15 wt % KOH solution) before being exhausted to a ventilated hood.

3. Results and Discussion

3.1. Channel Fabrication Using Nested KOH Etching

The flow distribution of the gas and liquid feeds in the scaled-out reactor hinges on the introduction of the two phases to each reaction channel through individual flow distributors, and hence it is essential to precisely control the geometry of these channels. Nested KOH etching made it possible to create a high density of merging channels of significantly different hydraulic diameters (50–650 μm), e.g., reaction channels and liquid distributors (Figure 4), on the same side of the silicon wafer with excellent control over their geometry (i.e., right- angle intersecting corners). It is well-known that low-stress silicon nitride does not etch at all in KOH, and hence can be regarded as a perfect masking material [4]. However, two different masking materials are necessary for nested KOH etching. In this work, silicon oxide was used successfully as a masking material even for wafer-through etches (650 μm deep), albeit a moderate extent of lateral undercutting of the mask was observed (Figure 4 a). The mask and actual dimensions of the reaction channels as well as gas and liquid distributors are shown in Table 1. The width of the distributors was about 12% larger than designed, while that of the reaction channels was 21% larger due to the simultaneous etching of these channels with the (deeper) liquid inlet slit. If needed, tighter tolerances could be achieved by compensating the mask undercut in future mask designs, a common strategy used in DRIE fabrication processes that require thick (~1 μm) silicon oxide layers. Photographs of completed devices are shown in Figure 5.

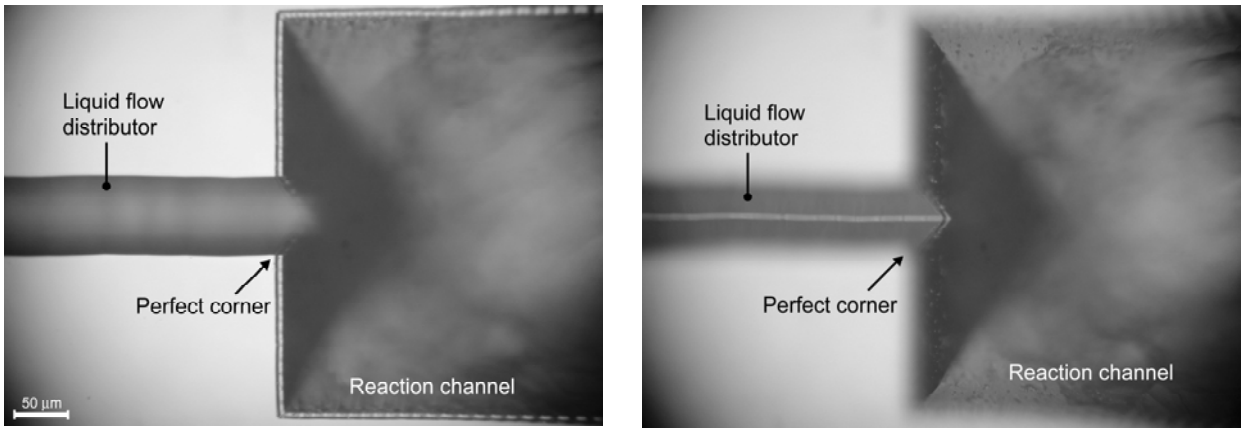

(a) (b)

Figure 4. Optical micrographs of the merger of a liquid distributor with its corresponding reaction channel. Images are in focus at (a) the top surface of the wafer and (b) the bottom of the ≈55-μm-deep liquid distributor immediately after the second etching step and before stripping the SiO_2 masking material. A slight lateral undercut of the silicon oxide mask is observed. The edge waviness of the distributor resulted from the use of 20-μm-resolution transparencies in the early stages of fabrication development to create the photomask plate prior to switching to the Mylar sheets. This waviness was present on the photomask and remained after the triangular cross section was terminated.

Table 1. Design and actual dimensions of the reaction channels and flow distributors in the scaled-out reactor.

Reactor component	Mask width, W (μm)	Actual width, W_{exp} (μm)	W_{exp}/W	d_h (μm)	$d_{h,exp}$ (μm)	A_{exp}/A^a
Reaction channel	400	484	1.21	207	250	1.46
Gas distributor	98	110	1.12	51	57	1.26
Liquid distributor	71	80	1.13	37	41	1.27

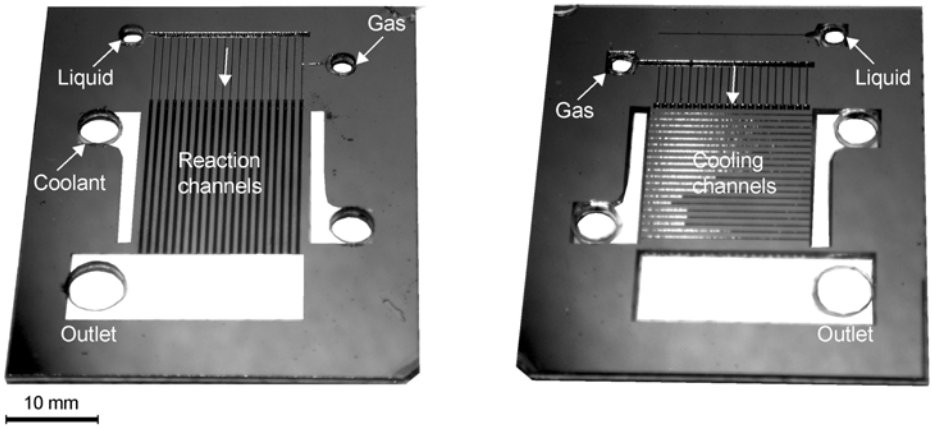

(a) (b)

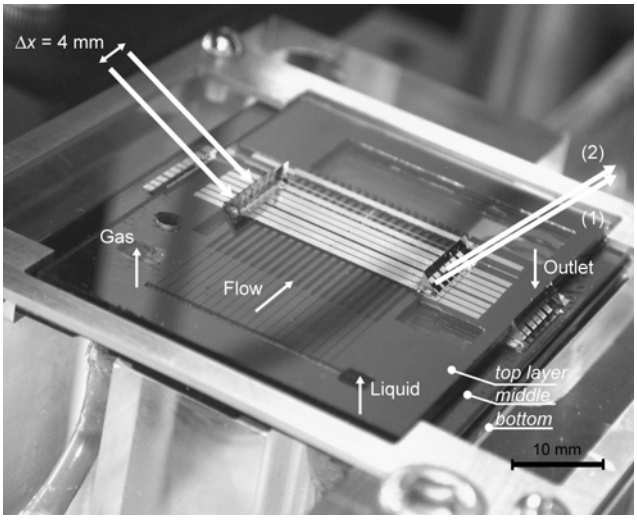

(c)

Figure 5. Photographs of (a) the front side of one silicon layer with the reaction channels and liquid distributors and (b) the back side with the gas access ports to the reaction channels, outlet slit, cooling slits, gas distributors, and cooling channels. Both sides of the silicon die are capped by Pyrex. (c) Photograph of a scaled-out device (three silicon and four Pyrex layers with Pyrex waveguides on the top and middle layers).

Defects observed on the silicon oxide mask etched as square features that were typically significantly smaller than any of the distributors (pitting). These pits intersected generally only one time per distributor and thus did not appreciably affect the overall etch uniformity or feature geometry, even

after etching through the 650-μm-thick silicon wafers, and did not impact the overall flow distribution [20]. On the other hand, unlike low-stress silicon nitride, the free-standing silicon oxide films that resulted from the through-etches were unstable and buckled due to internal compressive stress. A thickness of 100 nm of low-stress silicon nitride was sufficient to serve as a diffusion barrier during the thermal growth of 1.3–1.4-μm-thick silicon oxide films. Upon oxidation, although the most superficial layer of the nitride film became more difficult to etch in the CF_4-O_2 plasma, the underlying nitride film remained unaltered (etched at the same rate as as-deposited).

The etching rates of the various crystallographic planes of Si and SiO_2 selectivities in aqueous KOH have been documented in detail [4] and were used as a reference to select etching conditions. The requirements were an acceptable SiO_2 selectivity and good etch uniformity. The etch rate of (100) silicon is most sensitive to temperature but does not depend strongly on the KOH concentration for concentrations between 10 and 30 wt %. The etch rate of SiO_2, however, is sensitive to both temperature and solution concentration. Wafer-through etches (650 μm deep) at 60 ºC offered an acceptable SiO_2 selectivity, while we found that a 15 wt % solution prevented the formation of silicon islands at the bottom of the microchannels. Etches carried out in 10 wt % solutions at 60 ºC resulted in island formation in ~50% of the etched dies (Figure 6). The etch rate of (100) silicon in a 15 wt % solution at 60 ºC was measured to be 23–26 μm/h, with a (100) Si:SiO_2 selectivity of 675, comparable to the literature value of 736 [4]. Therefore, a 650-μm through etch required a minimum thickness of silicon oxide of 0.96 μm, and a thickness of 1.3–1.4 μm was used. The relatively thick silicon oxide layers (1.3 μm) used for the through etches introduced significant stress in the silicon wafer when the oxide thicknesses on the front and back sides of the wafer were not balanced. A thickness imbalance of 0.8 μm (0.5 and 1.3 μm on the front and back sides, respectively) resulted in extremely fragile wafers that did not survive the piranha clean after KOH etching. This problem was solved by simultaneously starting these etches.

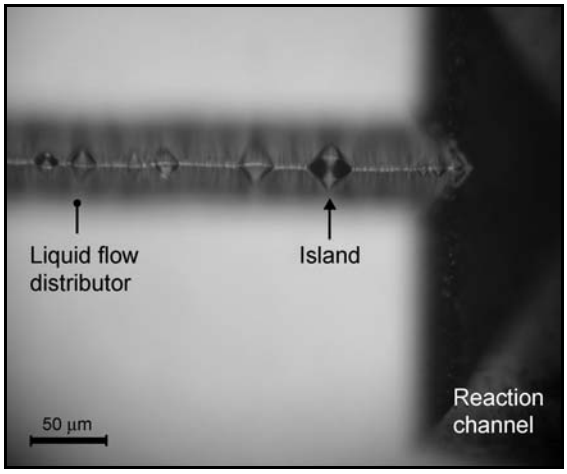

Figure 6. Silicon islands formed at the bottom of the liquid distributors when etched in 10 wt % KOH at 60 ºC. The optical micrograph is in focus at the bottom of the channel.

3.2. Characterization of Protective Films

3.2.1. Crystal Structure, Adhesion, Pinhole Density

To establish insight into the corrosion resistance of the nickel coatings, the following film properties were characterized: structure, adhesion, residual stress, pinhole density, surface chemical composition after anodic-bonding heating, step coverage, and elemental film chemical composition after fluorine exposure. Evaporated nickel films were polycrystalline with a face-centered cubic structure (lattice constant of 3.5 Å) and an average crystallite size of approximately 127 Å, estimated using the Scherrer formula without lattice strain correction. Changes in wafer bow caused by the deposition of the Ni/Cr films indicated that the films were tensile with a film stress of 516 MPa. The adhesion of the Ni/Cr films deposited on Pyrex was complete, i.e., no nickel peeled off from the surface upon removing the scotch tape. Films deposited on oxidized silicon (250-nm-thick SiO_2), however, were partially removed by the tape. Although no attempts to improve film adhesion were made for this work, the impact of partial Ni/Cr adhesion on SiO_2 on the long-term use of the microreactors should be evaluated.

Pinholes are frequently observed in evaporated films. Typical causes of pinhole formation are incomplete surface coverage (because of insufficient film thickness) and trace particle contamination

[26]. We found that evaporator cleanliness, in addition to film thickness, was a key process variable determining pinhole density. The lowest pinholes densities were achieved by using piranha- or Nanostrip-cleaned blank wafers to fill the unused slots on the evaporator plate. In addition, prior to film deposition, the evaporator plate and chamber were thoroughly vacuumed to remove any metal flakes from previous depositions. The pinhole density in Ni (200 nm)/Cr (10 nm) films was ≈3 holes/cm^2. Pinholes found in films deposited on Pyrex are shown in an inverted transmission optical micrograph in Figure 7. Correcting for the diffraction effects of the recording optics [30, 31], the diameter of these pinholes was estimated to be 1.5 μm. In thicker films, Ni (700 nm)/Cr (10 nm), the pinhole density was ≈1 hole/cm^2, and similar to that found in Au films of the same thickness, Au (700 nm)/Ti (10 nm). (The measured total film thickness of the Au films was 600 nm). Although thicker films resulted in fewer pinholes, the expected trade-off was larger residual internal stresses and perhaps lower film adhesion. Pinholes in the nickel film would expose the chromium adhesion layer, which would subsequently be susceptible to etching by fluorine, in particular in the gas inlets area. Cr is resistant to HF and is commonly used as a masking material for HF etching [25]. The coated area of the dual-channel reactor, ≈0.5 cm^2, was several orders of magnitude larger than the area where pinholes in Ni/Cr films were expected to be present. Although our microreactors did not show signs of film erosion over several hours of fluorination experiments, microreactor lifetime should continue to be monitored as a function of pinhole density.

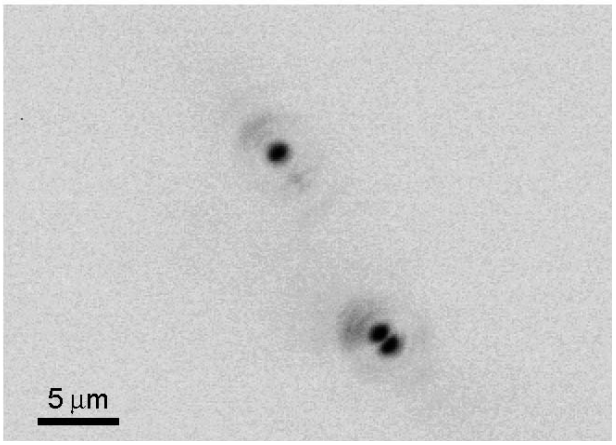

Figure 7. Inverted transmission optical micrograph showing pinholes on Ni (200 nm)/Cr (10 nm) films evaporated on Pyrex.

3.2.2. Heating

During wafer-level anodic bonding, temperature is ramped up from room temperature to 350 ºC over 14 min, held at 350 ºC for 4 min, and then ramped down from 350 to 250 ºC over 22 min. This heating may affect the film metal distribution because of enhanced solid diffusion and reaction at the interior film interfaces. Nickel silicides may form at the temperature of the anodic-bonding heating [32]. Excluding pinholes, the presence of silicon on the surface of a heated film deposited on a silicon substrate may point to a nickel silicide. From the measured pinhole densities, pinholes should not interfere with elemental surface analysis because the analysis area (up to 400 μm × 700 μm) is much smaller than the area where pinholes are likely to be found. Likewise, diffusion may occur at the Ni-Cr interface, and Cr may alloy with Ni. A nickel silicide would not be expected to form in films deposited on Pyrex, and the SiO_2 layer acts as a Ni-Si diffusion barrier. The effect of anodic-bonding heating on surface film composition was studied in films obtained from bonded microreactor chips (interior Pyrex walls and silicon from chip back side) as well as films deposited on silicon and heated without the application of an electrical potential. For both sets of samples, wafer heating was carried out under a nitrogen atmosphere.

Prior to bonding evaporated films had a uniform, golden color. Films deposited on the back side of silicon chips were in direct contact with the positive electrode during bonding. After bonding these films turned to a much darker, nonuniform, golden color. Films heated without the application of an electrical potential faced the nitrogen atmosphere and, in contrast, turned to an only slightly darker, uniform golden color. AES did not detect Cr or Si on samples obtained from bonded interior Pyrex walls. Carbon (from common hydrocarbon surface impurities), oxygen, and nickel were detected in a full (2,000 eV) kinetic energy scan. Oxygen was attributed to the presence of nickel oxide on the film surface. To

increase the AES Si sensitivity, a lower energy kinetic scan (1,000 eV) was performed, and Si was not detected either. Similarly, neither Cr nor Si was detected by AES on the back side of a bonded dual-channel reactor in which unoxidized Si was coated with Ni (200 nm)/Cr (10 nm) film. The AES Cr peaks partially overlap with those of oxygen. To increase the Cr sensitivity, XPS analysis of this film was performed, and Cr was not detected. The elemental surface analysis of Ni (200 nm)/Cr (10 nm)/SiO_2 (530 nm) films heated at 350 °C in the absence of an electric field was analyzed by XPS. Surveys were obtained before and after removing carbon from the surface using one sputtering cycle. A small sulfur impurity detected in the initial survey was also removed by the sputtering process. Except for sulfur and carbon, the same elements, nickel and oxygen, were observed in both spectra, and again neither Cr nor Si was detected. These results ruled out the presence of a nickel silicide on the film surface. Furthermore, because the elemental surface composition of nickel films did not change upon heating, the incorporation of fluorine in heated films is expected to occur in a similar fashion as in unheated films.

3.2.3. Step Coverage, Corrosion Resistance

The step coverage of Ni (200 nm)/Cr (10 nm) films over KOH-etched structures was examined in a 400-μm-wide triangular channel. Cross-sectional SEM showed similar wall coverage at the top and bottom of the channel (Figure 8). The channel cross-sectional scanning electron micrograph of a dual-channel reactor, in which the interchannel wall was Ni/Cr coated, showed that the metal pads did not prevent the silicon and Pyrex from coming into close contact during anodic bonding. The passivation of nickel films was investigated by exposing nickel-coated samples to a fluorine atmosphere for 2 and 8 hours and then analyzing their elemental surface composition by XPS. Upon fluorine exposure, the surface of Ni (200 nm)/Cr (10 nm)/SiO_2 (530 nm) films maintained its golden color and remained visually smooth. Carbon, oxygen, and nickel were detected before fluorine exposure. The same elements were detected on the surface after both exposure durations: carbon, oxygen, nickel, and fluorine.

Quantitative elemental analysis revealed similar surface chemical composition for both exposures. After the sputtering cycle that first removed carbon, atomic concentrations of approximately 10%, 30%, and 60% of fluorine, oxygen, and nickel, respectively, were obtained. The atomic concentrations in unexposed films were 15% oxygen and 85% nickel.

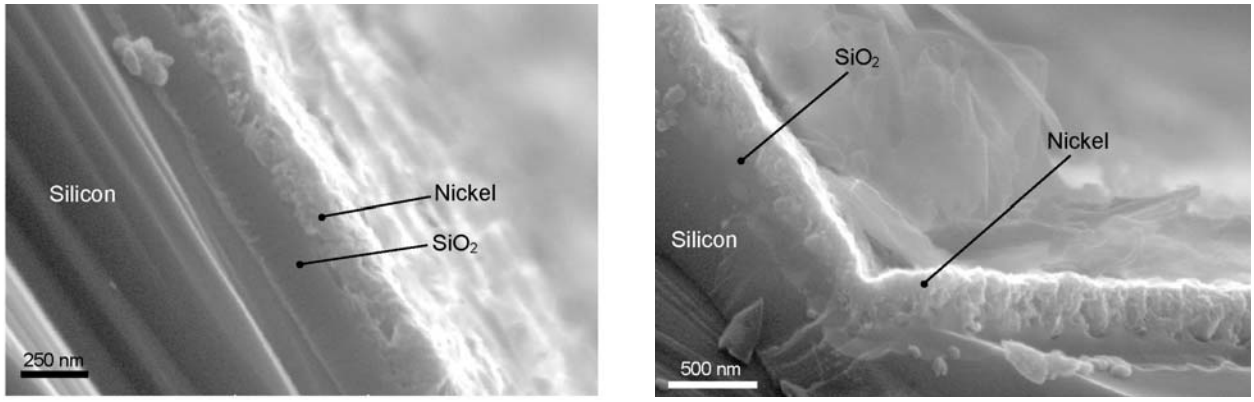

(a) (b)

Figure 8. Cross-sectional scanning electron micrographs showing the coverage of a Ni (200 nm)/Cr (10 nm)/SiO_2 (150 nm) film over a KOH-etched channel at (a) a channel wall close to the Pyrex cap and (b) the bottom of the channel. The anodic bonding temperature for this device was 500 °C. The contrast between the brighter Ni (metal) and SiO_2 (insulator) layers is sharp, and the interface between the two materials can be clearly distinguished.

To determine the extent of fluorine incorporation within the nickel film, several sputtering cycles were performed on films obtained before and after the 8 hours of fluorine exposure; carbon, fluorine, oxygen, and nickel signals were monitored after each cycle. Unexposed films showed single binding energy peaks for oxygen and nickel. Carbon was removed after one cycle. With increasing number of cycles, the concentration of oxygen gradually decreased while that of nickel increased, and no shifts in any of the binding energies were observed. In contrast, the initial survey of exposed films showed two binding energies for carbon and fluorine. After the first cycle, carbon was removed, and a single fluorine binding energy was observed. Oxygen exhibited a single binding energy. Upon fluorine exposure, the Ni

binding energy increased by 3.5 eV, while that of oxygen did not change. After the third cycle, the same Ni binding energy as that seen for unexposed films was observed. After the fifth cycle, fluorine was removed, and only oxygen and nickel remained. With increasing number of cycles, the concentration of oxygen decreased monotonically, while that of nickel increased, as observed for unexposed films. Similar patterns were observed for films exposed to fluorine for 2 hours.

The increase in Ni binding energy upon fluorine exposure was consistent with the formation of a nickel fluoride. The binding energy of Ni in NiF_2 is expected at 857–858 eV [33]. To compare this value with that obtained in our studies, the hydrocarbon carbon peak (expected at 285.0 eV) was used as a reference. The observed binding energies depend on the sample electrical conductivity, and hence small energy shifts (up to 3 eV) are common. To correct for this variability, the measured Ni binding energy was shifted by the same amount as that seen for carbon. The C peak in the unexposed film was at 284.2 eV. Therefore, 0.8 eV were added to the observed Ni energy, resulting in approximately 857 eV, in agreement with that of NiF_2. Passivation layers are typically a few nm thick. Given that the thickness examined by XPS is also on the order of a few nm (~20 atomic layers) [34], XPS was not suitable to quantitatively determine the thickness of the nickel film where fluorine was incorporated. Nevertheless, from the XPS depth profile of nickel films exposed to fluorine, we concluded that the incorporation of fluorine was confined within the original nickel oxide layer.

4. Conclusions

In conclusion, a nested KOH etching fabrication procedure was developed to build a multilayer, multichannel fluorination microreactor consisting of a large number of channels (60 reaction channels connected to individual gas and liquid distributors) of significantly different depths (50–650 μm) with precise control over their geometry. The fabrication procedure required four KOH etches. Uniform wafer-through etches with acceptable SiO_2:Si selectivity were obtained using 15 wt % KOH at 60 ºC. The wetted areas, with sloped channel walls, were coated with thermally grown silicon oxide and

electron-beam evaporated nickel films to protect them from the corrosive fluorination environment. Pyrex anodic bonding was used to cap the microchannels and stack the reaction layers. The average pinhole density in as-evaporated films was 3 holes/cm^2. These films presented good step coverage over the KOH-etched channels. Heating during anodic bonding (up to 325–350 °C for 4 min) did not significantly alter the film composition. Upon fluorine exposure, nickel films (200 nm) deposited on an adhesion layer of Cr (10 nm) over an oxidized silicon substrate (up to 500 nm SiO_2) led to the formation of a nickel fluoride passivation layer. Our microreactors were used to investigate direct fluorinations at room temperature in the annular-dry flow regime. No signs of film erosion were observed in the devices or near the gas ports after several hours of operation.

Acknowledgments

We thank Elisabeth L. Shaw of the MIT Center for Materials Science and Engineering (CMSE) for assistance with AES and XPS. This work was supported by the MIT Microchemical Systems Technology Center and made use of shared experimental facilities at the MIT CMSE.

References

1. Hartman, R.L., McMullen, J.P., and Jensen, K.F., Deciding Whether to Go with the Flow: Evaluating the Merits of Flow Reactors for Synthesis, *Angewandte Chemie International Edition*, **2011**, 50: 7502-7519.
2. de Mas, N., Günther, A., Schmidt, M.A., and Jensen, K.F., Microfabricated Multiphase Reactors for the Selective Direct Fluorination of Aromatics, *Industrial & Engineering Chemistry Research*, **2003**, 42 (4): 698-710.
3. McPake, C.B. and Sandford, G., Selective Continuous Flow Processes Using Fluorine Gas, *Organic Process Research & Development*, **2012**, 16: 844-851.
4. Seidel, H., Csepregi, L., Heuberger, A., and Baumgartel, H., Anisotropic Etching of Crystalline Silicon in Alkaline Solutions. 1. Orientation Dependence and Behavior of Passivation Layers., *Journal of the Electrochemical Society*, **1990**, 137 (11): 3612-3626.
5. Ayon, A.A., Braff, R., Lin, C.C., Sawin, H.H., and Schmidt, M.A., Characterization of a Time Multiplexed Inductively Coupled Plasma Etcher, *Journal of the Electrochemical Society*, **1999**, 146 (1): 339-349.
6. Ajmera, S.K., Delattre, C., Schmidt, M.A., and Jensen, K.F., Microfabricated Cross-Flow Chemical Reactor for Catalyst Testing, *Sensors and Actuators B-Chemical*, **2002**, 82 (2-3): 297-306.

7. Jerman, J.H., *Micromachining Process for Making Perfect Exterior Corner in an Etchable Substrate*, **1994**: US Patent 5,338,400.
8. Kwon, J.W. and Kim, E.S., Multi-Level Microfluidic Channel Routing with Protected Convex Corners, *Sensors and Actuators A-Physical*, **2002**, 97-8: 729-733.
9. Ajmera, S.K., Losey, M.W., Schmidt, M.A., and Jensen, K.F., Microfabricated Packed-Bed Reactor for Phosgene Synthesis, *AIChE Journal*, **2001**, 47 (7): 1639-1647.
10. Srinivasan, R., Hsing, I.M., Berger, P.E., Jensen, K.F., Firebaugh, S.L., Schmidt, M.A., Harold, M.P., Lerou, J.J., and Ryley, J.F., Micromachined Reactors for Catalytic Partial Oxidation Reactions, *AIChE Journal*, **1997**, 43 (11): 3059-3069.
11. Firebaugh, S.L., Jensen, K.F., and Schmidt, M.A., Investigation of High-Temperature Degradation of Platinum Thin Films with an In Situ Resistance Measurement Apparatus, *Journal of Microelectromechanical Systems*, **1998**, 7 (1): 128-135.
12. Kraus, T., Günther, A., de Mas, N., Schmidt, M.A., and Jensen, K.F., An Integrated Multiphase Flow Sensor for Microchannels, *Experiments in Fluids*, **2004**, 36 (6): 819-832.
13. Arana, L.R., Schaevitz, S.B., Franz, A.J., Schmidt, M.A., and Jensen, K.F., A Microfabricated Suspended-Tube Chemical Reactor for Thermally Efficient Fuel Processing, *Journal of Microelectromechanical Systems*, **2003**, 12 (5): 600-612.
14. Arana, L.R., de Mas, N., Schmidt, R., Franz, A.J., Schmidt, M.A., and Jensen, K.F., Isotropic Etching of Silicon in Fluorine Gas for MEMS Micromachining *Journal of Micromechanics and Microengineering*, **2007**, 17 (2): 384-392.
15. Jackman, R.J., Floyd, T.M., Ghodssi, R., Schmidt, M.A., and Jensen, K.F., Microfluidic Systems with On-Line UV Detection Fabricated in Photodefinable Epoxy, *Journal of Micromechanics and Microengineering*, **2001**, 11 (3): 263-269.
16. Lu, H., Schmidt, M.A., and Jensen, K.F., Photochemical Reactions and On-Line UV Detection in Microfabricated Reactors, *Lab on a Chip*, **2001**, 1 (1): 22-28.
17. Losey, M.W., Schmidt, M.A., and Jensen, K.F., Microfabricated Multiphase Packed-Bed Reactors: Characterization of Mass Transfer and Reactions, *Industrial & Engineering Chemistry Research*, **2001**, 40 (12): 2555-2562.
18. Günther, A., Jhunjhunwala, M., Thalmann, M., Schmidt, M.A., and Jensen, K.F., Micromixing of Miscible Liquids in Segmented Gas–Liquid Flow, *Langmuir*, **2005**, 21 (4): 1547-1555.
19. de Mas, N., Günther, A., Schmidt, M.A., and Jensen, K.F., Increasing Productivity of Microreactors for Fast Gas–Liquid Reactions: the Case of Direct Fluorination of Toluene, *Industrial & Engineering Chemistry Research*, **2009**, 48 (3): 1428-1434
20. de Mas, N., Günther, A., Kraus, T., Schmidt, M.A., and Jensen, K.F., Scaled-Out Multilayer Gas−Liquid Microreactor with Integrated Velocimetry Sensors, *Industrial & Engineering Chemistry Research*, **2005**, 44 (24): 8997-9013.
21. Sharpe, A.G., *Inorganic Chemistry,***1981**, London: Longman Group Limited.
22. *Ullmann's Encyclopedia of Industrial Chemistry,***1985**, New York: Wiley-VCH.
23. *Methods of Organic Chemistry (Houben-Weyl),***1999**, New York: Georg Thieme Verlag.
24. *Kirk-Othmer Encyclopedia of Chemical Technology,* 4th ed.,**1994**, New York: Wiley.
25. Kovacs, G.T.A., *Micromachined Transducers Sourcebook,***1998**, Boston: WCB/McGraw-Hill.
26. Christensen, C., de Reus, R., and Bouwstra, S., Tantalum Oxide Thin Films as Protective Coatings for Sensors, *Journal of Micromechanics and Microengineering*, **1999**, 9 (2): 113-118.
27. Steyn, J.L., Hydraulic Amplification for Actuation in Microelectromechanical Systems, **2002**, Massachusetts Institute of Technology, Department of Aeronautical and Astronautical Engineering, M.S. Thesis, Cambridge, MA.

28. Hidber, P.C., Helbig, W., Kim, E., and Whitesides, G.M., Microcontact Printing of Palladium Colloids: Micron-Scale Patterning by Electroless Deposition of Copper, *Langmuir*, **1996**, 12 (5): 1375-1380.
29. Ohring, M., *The Materials Science of Thin Films,***1992**, London: Academic Press.
30. Santiago, J.G., Wereley, S.T., Meinhart, C.D., Beebe, D.J., and Adrian, R.J., A Particle Image Velocimetry System for Microfluidics, *Experiments in Fluids*, **1998**, 25 (4): 316-319.
31. Meinhart, C.D. and Wereley, S.T., The Theory of Diffraction-Limited Resolution in Microparticle Image Velocimetry, *Measurement Science & Technology*, **2003**, 14 (7): 1047-1053.
32. Tu, K.N., Mayer, J.W., and Feldman, L.C., *Electronic Thin Film Science for Electrical Engineers and Material Scientists,***1992**, New York: Macmillan Publishing Company.
33. Wagner, C.D., Naumkin, A.V., Kraut-Vass, A., Allison, J.W., Powell, C.J., and Rumble Jr., J.R., *NIST X-Ray Photoelectron Spectroscopy Database. NIST Standard Reference Database 20, Version 3.4 (Web Version),***2003**.
34. *Encyclopedia of Materials Characterization: Surface, Interfaces, Thin Films,***1992**, Boston: Butterworth-Heinemann.